Carrier recombination mechanism in CsPbBr_{3} revealed by time-resolved photoluminescence spectroscopy

J. A. Peters, Zhifu Liu, Ruihan Yu, K. M. McCall, Yihui He, M. G. Kanatzidis, and B. W. Wessels

Phys. Rev. B **100**, 235305 — Published 12 December 2019

DOI: 10.1103/PhysRevB.100.235305

Carrier recombination mechanism in $CsPbBr_3$ revealed by time resolved photoluminescence spectroscopy

J. A. Peters,[1, 2] Zhifu Liu, [1] Ruihan Yu, [1] K. M. McCall, [3] Yihui He, [3] M. G. Kanatzidis, [3]

and B. W. Wessels[1, *]

[1]*Department of Materials Science and Engineering, Northwestern University, Evanston, IL 60208*
[2] *Department of Chemistry and Physics, Chicago State University, Chicago, IL 60608*
[3]*Department of Chemistry, Northwestern University, Evanston, IL 60208*

Revised Sept. 4, 2019

Abstract

We systematically investigate the recombination mechanism of photogenerated charge carriers in bulk $CsPbBr_3$ by means of time-resolved photoluminescence (TR-PL) spectroscopy at low temperature and various laser excitation powers. A dynamic recombination model is proposed to describe the TR-PL that predicts the time dependent exciton and free charge populations. It provides a clear representation of competing mono- and bi-molecular recombination processes. A decrease in carrier lifetime with increasing laser intensity was observed that was attributed to exciton-exciton scattering. A bimolecular recombination coefficient of $\sim 10^{-7}$ cm^3/s was obtained for exciton recombination. As the concentration of photoexcited carriers increases, stronger exciton-exciton annihilation occurs. The exciton–exciton annihilation rate for $CsPbBr_3$ is 3.63×10^{-7} cm^3 s^{-1} at 10 mW laser power. Notably, the exciton–exciton annihilation rate in bulk material is comparable to that obtained for photoexcited $CsPbBr_3$ nanoscale quantum dots.

I. INTRODUCTION

The demand for low cost, high energy resolution, and stable detector materials has significantly increased over the past two decades for applications in homeland security, nonproliferation, and national defense. For X-ray and γ-ray detection, compound semiconductors have a number of distinct advantages over their elemental counterparts, most of which arise from the wide range of stopping powers, wide band gaps available and room temperature operation. Current hard radiation semiconductor detectors used in spectroscopic measurements of γ -rays rely on expensive materials such as CdZnTe crystals. Despite their advantages, however, only a handful of semiconductor materials are currently being considered in radiation detection due to the strict demands on the properties that include a high band gap (>1.5 eV) to minimize dark current, high average atomic number and a high mobility-lifetime ($\mu\tau$) product [1, 2, 3, 4].

One of the major challenges in producing detector-grade materials is the difficulty of growing chemically pure and structurally perfect crystals with exact stoichiometry. We have identified and are developing a variety of promising wide gap semiconductors for room temperature radiation detection in the *x*-ray and 60 - 662 keV gamma ray regimes [5, 6, 7]. Candidate detector compounds under investigation include $CsPbBr_3$ and $TlSn_2I_5$. We have also identified several low-cost compound semiconductors including $Pb_2P_2Se_6$ and $Hg_3Se_2I_2$ and are investigating their spectral responses to 122 keV γ-radiation and beyond. Our studies show that their band gaps, resistivity values, mobility-lifetime products, and *x*-ray response are approaching those of the benchmark detector material CdZnTe.

$CsPbBr_3$ has recently shown very promising results in room temperature radiation detection [8]. The easily scalable crystal growth and high-energy gamma ray resolution

underscore the importance of $CsPbBr_3$ as a next generation material for room temperature radiation detection. Besides high energy radiation detection capabilities of $CsPbBr_3$, it also showed promise for solar cells [9]. The compound is a direct bandgap (at the Γ point) semiconductor that crystallizes in the three-dimensional (3D) perovskite structural type [10]. $CsPbBr_3$ planar detectors achieved remarkable energy resolving capabilities. Specifically, the $CsPbBr_3$ detector resolved the 59.5 keV (^{241}Am γ-ray), 122 and 136 keV (^{57}Co γ-ray), 511 keV (^{22}Na γ-ray), and 662 keV (^{137}Cs γ-ray) lines with best spectral resolution of ~3.8% [8]. $CsPbBr_3$ is unique among gamma-ray detection materials in that its hole transport properties are responsible for the high performance. The superior mobility-lifetime product for holes (1.34×10^{-3} cm^2 V^{-1}) derives mainly from the record long hole carrier lifetime (~ 25 μs) [8].

To improve the detector performance, high mobility-lifetime products are required. Furthermore, native defects/impurities within specific samples need to be identified and be reduced/eliminated. A recent report indicated that the compound may be insensitive to defects within a relatively wide energy range [11]. However, for further development of the perovskite $CsPbBr_3$ it is essential to gain a thorough understanding of what limits the charge carrier transport in the material. The effectiveness of a radiation detector or any optoelectronic device mostly depends on the ability of the material to generate long lived, free charge carriers, and therefore must have low concentrations of electronic defects/impurities. The lifetime of the charge carriers is determined by electron and hole recombination. Hence, determining the origin of radiative and nonradiative decay lifetimes of these carriers and having a detailed understanding of carrier recombination processes are essential both to further our understanding and to reach the ultimate potential of these materials for both radiation detection and

optoelectronic applications. One of the most versatile techniques for characterizing charge carrier dynamics and evaluating the fundamental optical properties of semiconductor materials is time-resolved optical spectroscopy. The carrier transport and carrier-recombination processes in various perovskites have been extensively studied by means of time-resolved photoluminescence (TR-PL) [12, 13]. Time-resolved photoluminescence is a nondestructive technique for probing the effects of impurities/defects within semiconductor samples with potential for room temperature radiation detection. TR-PL has the capability of separating defect luminescence involved in mono- and bi-molecular recombination processes, thereby screening promising radiation detection candidates [14]. In addition, it provides an opportunity for understanding carrier dynamics and recombination. Parameters that determine crystal quality include the densities of electrons, holes, excitons, and unintended imperfections.

In this report, we investigate the nature and dynamics of photogenerated charge carriers in bulk $CsPbBr_3$ by means of TR-PL spectroscopy at various laser excitation powers. We report on the temperature dependence and excitation intensity dependence of the time-resolved PL. Since PL of $CsPbBr_3$ originates from recombination of charge carriers and excitons, its time and temperature dependencies enable indirect evaluation of photogenerated carrier dynamics [12]. The photocarrier dynamics are well described by a simple rate equation including single-carrier recombination and electron−hole exciton recombination. Our studies allowed us to separate the monomolecular and bimolecular recombination contributions and predict the ratio between exciton and free charge populations. At all intensities, the time evolution of the transient PL was dominated by bimolecular recombination. Determining the origin of radiative and non-radiative decay and gaining a detailed understanding of charge generation and recombination within the

halide perovskite $CsPbBr_3$ are essential to understanding and developing these materials. Nonequilibrium carrier lifetime is an important material parameter that influences the performance of radiation detector and optoelectronic devices.

II. EXPERIMENT

The crystal growth procedure and the experimental details are described below.

$PbBr_2$ synthesis: For the sample used in this paper (ID: KM11, $CsPbBr_3$, solid-state), 66.24 g (200 mmol) of $Pb(NO_3)_2$ was dissolved in 150 mL of boiling deionized water, and 47.51 g (400 mmol) of KBr was dissolved in 75 mL of water in a separate beaker. The KBr solution was slowly added to the lead nitrate solution under stirring, leading to immediate precipitation of white $PbBr_2$. After cooling to room temperature, the solid was filtered through a fritted-dish funnel under vacuum, washed copiously with distilled water, and dried overnight under vacuum. For removal of insoluble impurities, the dried product was dissolved in 18 g batches in 1000 mL of ultrapure (Millipore) water and filtered under vacuum. The solid was filtered through a fritted-dish funnel under vacuum and heated in a vacuum oven at 50 ºC to remove water. The final yield was 66 g (~90%).

Solid-State Synthesis and Bridgman Growth of $CsPbBr_3$ single crystals: $CsPbBr_3$ was synthesized via a solid-state reaction and single crystals were grown using Bridgman methods and polished for optical measurements. These procedures are described in detail elsewhere [15]. In short, stoichiometric amounts (40 mmol) of $PbBr_2$ (prepared as above) and CsBr (purchased from Sigma Aldrich, 5N) were ground together and flame-sealed in a quartz ampule under vacuum and reacted in a box furnace at 650 ºC. The resulting $CsPbBr_3$ was powdered and used for Bridgman

growth in a two-zone Bridgman furnace with zone temperatures of 800 ºC and 400 ºC and a translation speed of 2 mm/h. Wafers were cut with a diamond saw and dry-polished to mirror-like surfaces using silicon carbide sandpaper, then rinsed with toluene to remove stray powder. The crystals are not intentionally doped and tend to be *p*-type in nature. Previous density functional theory (DFT) calculations indicate that under Pb-poor growth conditions Pb vacancies and Cs on Pb antisite native defects form shallow acceptor levels in the material. This results in low intrinsic electron carrier density, thereby making the material quasi p-type [10,11].

Steady-State Photoluminescence and Time-Resolved Photoluminescence (TRPL) spectroscopy: Steady-state PL spectra were measured using a 405-nm line from a CW semiconductor diode laser (OBIS laser) with the beam diameter of ~0.8 mm. The intensity of the laser was ~100 mW/cm^2. The spectra were resolved by a 500M SPEX grating monochromator equipped with a Hamamatsu photomultiplier tube (R928 PMT) and collected in the wavelength range 400□600 nm at a rate of 0.5 nm/s. A 405-nm bandpass filter (Thorlabs, Inc.) with a FWHM of 10 nm was used to deliver a narrower laser line to the sample. For the TR-PL measurements the $CsPbBr_3$ perovskite crystal is illuminated with the 405-nm light pulses operated at 20 Hz as shown in Fig. 1. The pulse width was kept at 1 microsecond and the spot size is 1 mm^2. Excitation intensities were adjusted using optical density filters and the laser power was varied in the range between 10 mW and 75 mW. The laser pulse is targeted on the sample within a cryostat chamber. The temperature inside the cryostat was controlled by a temperature controller with helium gas as the cooling agent. Luminescence from the bulk sample was collected by the lenses and focused on the entrance slit of a spectrophotometer. The PL is spectrally resolved by a SPEX

monochromator by Horiba (model number SPEX 500M, with a grating of 1200 grooves/mm, a dispersion of 1.6 nm/mm, and a resolution of 0.02 nm) and detected by a PMT (Hamamatsu R955).

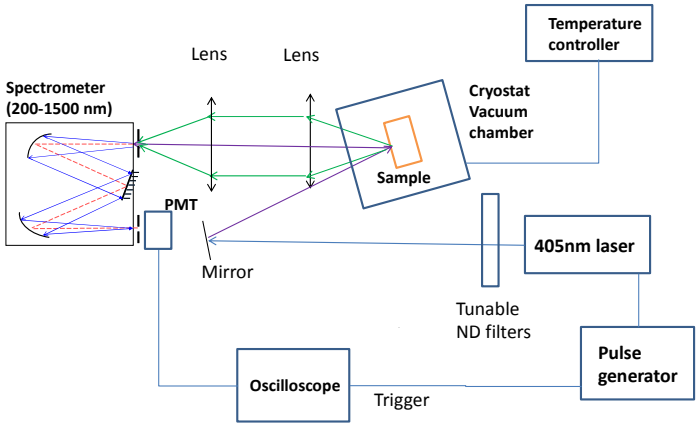

Fig. 1. Schematic of the setup for the TR-PL measurement.

III. RESULTS AND DISCUSSION

Fig. 2a shows the temperature-dependent steady state PL spectra of the $CsPbBr_3$ crystal obtained from 17 K to 295 K. The PL spectra were obtained under an excitation of ~1 mW 405 nm semiconductor diode laser light dispersed with a grating monochromator. At low temperatures, ≤ 80 K, a shoulder on the low-energy side becomes observable. At higher temperatures, ≥ 150 K, the PL spectra display a single dominant high energy peak. Fig. 2b shows the decomposition of the spectrum at 17 K using standard Gaussian profile fitting. Two emission bands are resolved, a broad band (~28 nm width) centered at 2.26 eV and a narrow band (~ 6nm width) centered at 2.29 eV. These emissions (peaks 1 and 2 in fig. 2b) have been previously observed in $CsPbBr_3$ bulk single crystals [16] and $CsPbBr_3$-like quantum dots in CsBr single crystals [17]. In Ref. [16], only peak 2 was observed and it was attributed to excitons bound to intrinsic defects. However, in Ref. [17] both emission peaks were observed and attributed to excitonic emissions based on the excitation

power dependences of the two PL emissions. Specifically, peak 2 on the high-energy side was ascribed to the emission of free excitons [16, 17], whereas Peak 1 was ascribed to the radiative recombination of excitons bound to Br vacancy centers acting as trapping centers within the $CsPbBr_3$ lattice [17]. We also observe from Fig. 2a that the position of both peaks essentially blueshifts monotonically with increasing temperature over the entire temperature range. The anomalous temperature dependent behavior of the PL peaks was previously determined to be due to thermal expansion and thermal redistribution of trapped excitons [16].

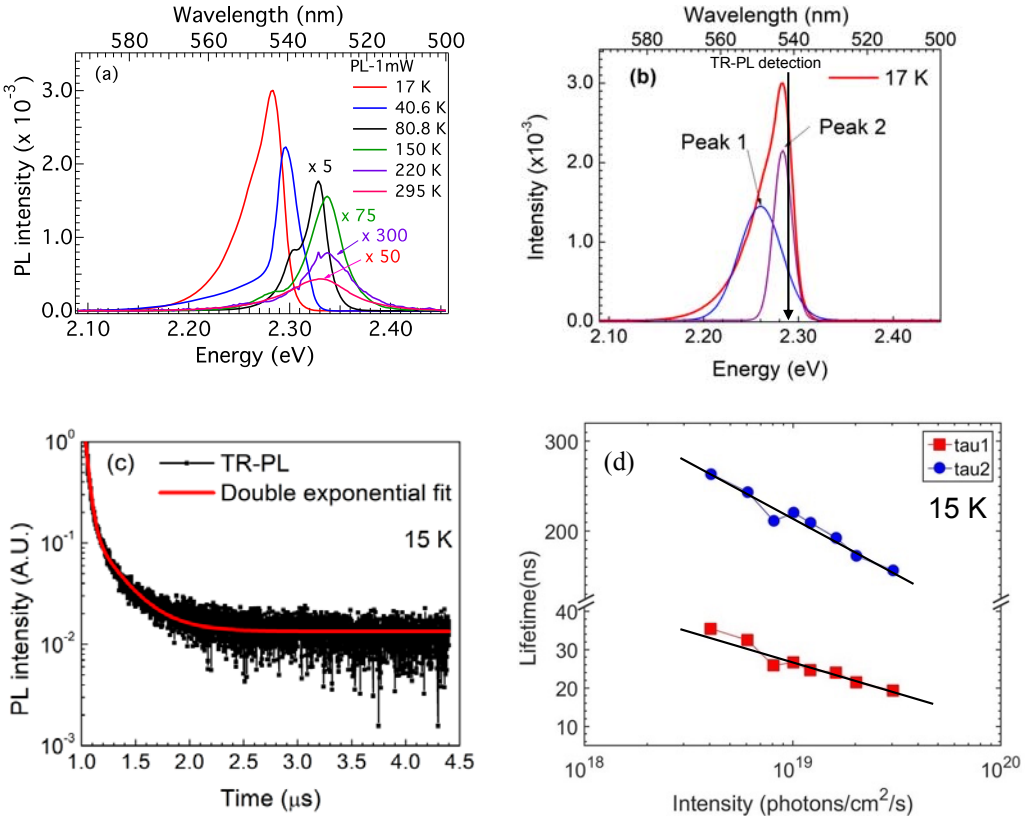

Fig. 2. (a) PL spectra of $CsPbBr_3$ at different temperatures under an excitation of ~1 mW 405 nm light from a semiconductor diode laser. (b) PL at 17 K showing the two emission peaks. (c) Time-resolved PL decay curve (plotted on a semi-logarithmic scale) of emission peak 2 obtained at 15 K. Solid line is the fitting curve with a bi-exponential decay function (as described in the text) (d) Results of fitting double exponential decay times of PL monitored vs. power of laser. The laser pulse duration was kept at 1 μs. The cryostat temperature was kept at 15 K, and the peak of the TR-PL was at a wavelength of ~541 nm.

To analyze the nature of the PL peak emissions, TR-PL decay curves were measured at 15 K. A typical representative decay for peak 2 (541 nm) at 10 mW laser power is illustrated in Fig. 2c. We found out that in all cases reported here, the decay profile could not be adequately described by a single-exponential function, with a characteristic PL lifetime, but requires a linear combination of exponential functions with different characteristic decay times. The time dependence of the luminescence intensity I(t) observed in Fig. 2c can be described as a sum of exponential decay functions given by $I(t) = C_1\exp(-t/\tau_1) + C_2\exp(-t/\tau_2)$, where C_1, and C_2 are scaling parameters.

The measured decay curves at 541 nm (Fig. 2c) for various excitation intensities (10 mW to 75 mW) are fitted with a double exponential function. The smooth solid line represents the fitting curve with a short time constant (τ_1 = 36.8 ns) and a long time constant (τ_2 = 268 ns) for an excitation intensity of 10 mW. Both the shorter (τ_1) and longer (τ_2) decay times decrease with increasing excitation intensity (Fig. 2d). We note that even though the fitting parameters change for a multi-exponential fitting, two invariants, $C_{sum} = \sum C_i$ and $1/\tau_{ave} = \sum C_i/\tau_i$, exist. The first invariant is the initial value of the decay while the second invariant is the initial value of the decay rate (slope), where "initial" is defined as the instant the excitation pulse ends. We normalized each dataset and the fit was then conducted with the natural constraints applied. No weight was used for the fit. The amplitude C_1 is ~75% of the total decay, $\sum_i C_i$. Since for all excitation intensities, the derivative of TR-PL with respect to time at $t = 0$ should be the same, we obtained the second invariant ($\tau_{ave} = \frac{1}{\frac{C_1}{\tau_1}+\frac{C_2}{\tau_2}}$,) for a two-exponential decay model. These invariants (C_{sum} and $1/\tau_{ave}$) can be used as links between the empirical models and a dynamic kinetic model, described later.

The need for at least a bi-exponential decay function and two characteristic decay times (Fig. 2d) indicates there are at least two kinetically distinct processes [18] that decay either radiatively or nonradiatively and contribute to the PL decay observed in Fig. 2c. However, the excitation intensity dependence of these decay times (Fig. 2d) points to other complex processes, the origin of which is presently unknown but is under further investigation. It is worth noting here that although multi-exponential fitting provides a convenient means of representing the shape of a decay curve, each of the components may not necessarily be associated with a separable physical mechanism and therefore a detailed dynamic kinetic analysis is required.

(i) Recombination theory and carrier kinetics

To probe the nature of carrier dynamics in $CsPbBr_3$ and provide detailed information on the recombination kinetics of the carriers, the intensity dependence of TR-PL decay curves was studied. The theory of transient PL was extensively reviewed by Stranks et al. [19, 20]. Here we extend the theory to include exciton-exciton annihilation, which is presumably strong in the $CsPbBr_3$ sample investigated. In brief, under steady state conditions (when the PL signal has reached a nearly constant value) an optical pulse excitation generates an electron-hole pair density of N_0 at time $t = 0$ (defined by the end of the excitation pulse). N_0 represents the initial photogenerated electron-hole pair density from the optical pulse excitation, which does not include the thermal equilibrium concentrations of the carriers. N_0 is calculated using the incident photon energy, laser power, laser spot size, and absorption length. Our estimation shows that the absorption length is ~ 0.1mm, which is ~10 % of the sample thickness. Also, in our analysis we did not consider the effect of carrier diffusion.

Following photoexcitation free charge carriers are excited into higher-lying states in the conduction band (CB) and then immediately decay to the bottom of the CB due to electron-phonon scattering. These photogenerated free carriers may form excitons or immediately recombine. Electronic traps may also be populated. The excitons can recombine radiatively or dissociate into free electrons and holes. With increasing laser intensity, excitons will interact with each other and exciton-exciton annihilation will occur [21]. Exciton-exciton annihilation is a many-body interaction in which one exciton (or electron−hole pair) is destroyed and its energy transferred to another exciton. This annihilation pathway is the excitonic analog of the Auger recombination process and hence nonradiative recombination can occur via exciton−exciton annihilation [22].

Under photoexcitation N_0 electron-hole pairs are created with N_0 electrons and N_0 holes that are greater than their steady state equilibrium concentrations. The total concentration of photogenerated electrons N_0 is thus comprised of free electrons (n_e) and excitons (n_x) i.e. $N_0 = n_e(0) + n_x(0)$, but excludes trapped carriers. In the presence of available traps the hole concentration (n_h) will be related to electron concentration (n_e) by $n_h(0) = n_T + n_e(0) = N_0 - n_x(0) + n_T$, where n_T is the density of filled traps. The equilibrium carrier concentration can be described by a generalized form of the Saha equation [19, 20] for *p*-type materials (such as $CsPbBr_3$ crystals) as $(n_h - n_T) \cdot n_h - A.(N_0 + n_T - n_h) = 0$. The same formalism holds for *n*-type materials. The solution to this equation yields a value for hole density n_h given by $n_h(0) = -\frac{(A-n_T)}{2} + \frac{1}{2}\sqrt{(A+n_T)^2 + 4AN_0}$. The value of the parameter $A = \nu_x/\nu_e\nu_h \, exp(-E_b/k_BT)$ depends on the temperature T and exciton binding energy E_b and it is independent of the photogenerated density N_0. $\nu_i = \lambda_i^3$, is the volume occupied by each

carrier (electrons, holes, or excitons) with λ_i being the thermal wavelength. Considering that undoped $CsPbBr_3$ crystals are intrinsically *p*-type in nature, the condition $4AN_0 \ll (A + n_T)^2$ is assumed to be valid, leading to $n_h(0) \approx n_T + \frac{A \cdot N_0}{(A+n_T)}$, $n_e(0) \approx \frac{A \cdot N_0}{(A+n_T)}$, and $n_x(0) \approx \frac{N_0 \cdot n_T}{(A+n_T)}$.

An extended kinetic model that accounts for exciton formation, annihilation, and dissociation into free charges, as well as trapping of free carriers is given by the rate equations [19, 20]:

$$\left.\begin{aligned} \frac{dn_e}{dt} &= R_d n_x - R_f n_e n_h - R_{eh} n_e n_h - R_{pop} n_e (N_T - n_T) \\ \frac{dn_x}{dt} &= R_f n_e n_h - R_d n_x - R_x n_x - \gamma {n_x}^2 \end{aligned}\right\} \quad (1)$$

where R_d is the rate of exciton dissociation into free electron-hole pairs, R_f of exciton formation from free electron-hole pairs, R_{pop} is the trap population rate constant, N_T is the total carrier trap density, n_T is the filled trap density, R_{eh} is the recombination rate of free electron-hole pairs, and R_x is the rate of exciton decay. The term $\gamma {n_x}^2$ represents the exciton-exciton annihilation term. Using the condition that under thermal equilibrium $An_x = n_e n_h$, equation 1 can be simplified to obtain

$$\frac{d(n_e+n_x)}{dt} = \frac{dN(t)}{dt} = -\frac{\gamma_0}{A} n_e n_h - R_{pop} n_e (N_T - n_T) - \gamma {n_x}^2 \quad (2)$$

where $\gamma_0 (= AR_{eh} + R_x)$ accounts for the total rate of electronic decay not involving traps. If we define a normalized photogenerated carrier concentration x as $x = N(t)/(A + n_T)$, the hole, electron, and exciton concentrations now become $n_e(t) \approx Ax$, $n_h(t) \approx n_T + Ax$, $n_x(t) \approx xn_T$, respectively. For the current discussion, we have assumed that $(A + n_T)$ is constant for a given power of laser that the sample is exposed to. Consequently, Eq. (2) now becomes:

$$\left.\begin{aligned} \frac{dx}{dt} &= -\frac{A\gamma_0}{(A+n_T)}\left[\frac{n_T}{A} + \frac{R_{pop}(N_T - n_T)}{\gamma_0}\right] x - \frac{A\gamma_0 + \gamma {n_T}^2}{(A+n_T)} x^2 \\ \frac{dx}{dt} &= -\frac{AC_1\gamma_0}{(A+n_T)} x - \frac{A\gamma_0 + \gamma {n_T}^2}{(A+n_T)} x^2 \end{aligned}\right\} \quad (3)$$

where $C_1 = \frac{n_T}{A} + \frac{R_{pop}(N_T - n_T)}{\gamma_0}$.

The time evolution of the normalized photogenerated carrier concentration *x* therefore follows the equation given by:

$$\frac{dx}{dt} = -k_1 x - Bx^2 \quad (4)$$

with $k_1 = 1/\tau$ and $B = \frac{A\gamma_0 + \gamma {n_T}^2}{(A + n_T)}$. For free carriers, k_1 is the monomolecular decay rate, indicative of free carrier trapping, and *B* is the rate constant associated with electron-hole recombination. In the case of excitons, k_1 represents the monomolecular excitonic and/or trap-assisted recombination and *B* is the exciton−exciton annihilation coefficient. The solution to Eq. (3) is given by

$$x = \frac{x_0 e^{-\frac{t}{\tau}}}{1 + B x_0 \tau (1 - e^{-\frac{t}{\tau}})} \quad (5)$$

In the time derivative of the carrier concentration given in Eq. (3), the first term is the monomolecular contribution, and the second term is the bimolecular contribution. The ratio of the bimolecular term over the monomolecular term is $Bx\tau$, which decays with time *t*. Therefore, no matter what the initial contribution of the bimolecular term is, its contribution decays with time, and the monomolecular term should ultimately prevail. If $Bx_0\tau > 1$, there will be a cross over when $Bx\tau = 1$. The cross over time depends on the characteristic parameter τ.

Fig. 3 shows the normalized PL decay dynamics under different excitation intensities. For free carriers, the radiative decay rate is proportional to the product of the densities of free electrons and free holes. For free excitons, the radiative decay rate is proportional to the density of free excitons. Since the two processes take place in parallel a net radiative decay rate can be assumed,

which is proportional to the photoluminescence intensity. Hence, the time-dependent normalized PL intensity can be written as:

$$\frac{I_{eh}^{PL}(t)}{I_{eh}^{PL}(0)} = \frac{I_{x}^{PL}(t)}{I_{x}^{PL}(0)} = \frac{n_e(t)*n_h(t)}{n_e(0)*n_h(0)} \tag{6}$$

Using Eq. (5) and the expressions for n_e and n_h given above, equation 6 can be written as

$$\left.\begin{aligned} \frac{I_{eh}^{PL}(t)}{I_{eh}^{PL}(0)} &= \frac{1}{[n_T+Ax_0]*Ax_0}*\left[n_T+\frac{Ax_0e^{-\frac{t}{\tau}}}{1+x_0B\tau\left(1-e^{-\frac{t}{\tau}}\right)}\right]*\frac{Ax_0e^{-\frac{t}{\tau}}}{1+x_0B\tau\left(1-e^{-\frac{t}{\tau}}\right)} \\ &= \frac{1}{1+a}*\left[1+\frac{ae^{-t/\tau}}{1+b'\left(1-e^{-\frac{t}{\tau}}\right)}\right]*\frac{e^{-t/\tau}}{1+b'\left(1-e^{-\frac{t}{\tau}}\right)} \end{aligned}\right\} \tag{7}$$

where $a = Ax_0/n_T,\ b' = x_0B\tau$. Hence eqn. 7 is reduced to include 3 independent fitting parameters (a, b', and τ).

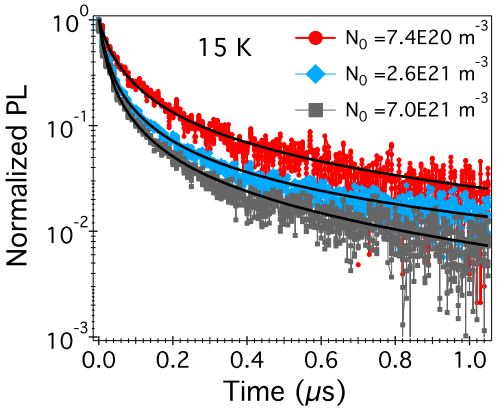

Fig. 3. PL intensity [monitored at ~2.29 eV (541 nm)] as a function of time after pulsed excitation (405 nm, 20 Hz repetition rate) for a $CsPbBr_3$ crystal at 15 K with different initial photoexcitation densities N_0. Solid lines are fits to the experimental data (noisy lines) for the model [Eq. (7)].

The normalized TR-PL decays were globally fitted to the model expressed in Eq. (7) by the method of least squares for the various excitation intensities. No weighting was applied to the parameters. The fit was performed on a linear scale, and plotted on a semilog scale. The resulting

fitting parameters *a*, *b'*, and τ (Table 1) were obtained from the model and the monomolecular decay coefficient ($k_1 = 1/\tau$) was determined to be ~ 2×10^6 s^{-1}. We can extract (at the various excitation intensities) steady state values for the filled trap concentration n_T, hole concentration n_h (0), electron concentration n_e (0), and exciton density n_x (0). By using the fitting parameter ***a*** in combination with the calculated values of N_0 and A, the trap density n_T is deduced from the equation $\boldsymbol{a} = \frac{A}{n_T} \cdot \frac{N_0}{(A+n_T)}$. The value of x_0 is then deduced from the equation $x_0 = N_0/(A + n_T)$. Consequently, the concentrations n_e (0) and n_h (0) are determined by using the approximate relationships $Ax_0 = n_e(0)$ and $n_h(0) = n_e(0) + n_T$. The results are given in Table 1, where Column 7 = Column 5 + Column 6. The values of the exciton concentration n_x (0) shown in Column 8 are obtained from the equation $N_0 = n_e(0) + n_x(0)$.

Table 1. Fitting results from Eq. (7) that show values of the parameters *a*, *b'*, and τ as well as trap and carrier concentrations

Intensity (mW)	***a***	***b′***	**τ (μs)**	n_T (× 10^{14} **cm**$^{-3}$)	n_e **(0)** (× 10^{12} **cm**$^{-3}$)	n_h **(0)** (× 10^{14} **cm**$^{-3}$)	n_x **(0)** (× 10^{14} **cm**$^{-3}$)
10	0.463	8.14	0.477	1.07	0.95	1.08	0.49
15	0.593	10.46	0.496	1.10	1.22	1.11	0.64
20	0.737	11.17	0.494	1.19	1.51	1.21	0.86
25	1.081	10.06	0.442	0.957	2.21	0.98	1.01
30	1.264	10.71	0.467	1.00	2.59	1.03	1.24
40	1.467	11.41	0.467	1.19	3.01	1.22	1.71
50	1.594	11.97	0.453	1.62	3.29	1.66	2.56
75	2.719	10.83	0.436	1.71	5.61	1.77	4.59

The extracted trap density values n_T in Table 1 are nearly constant, and are also nearly the same as the hole concentration. Moreover, they are within the same order of magnitude with

those obtained by M. Zhang et al. for a total trap density $N_T = 3.84 \times 10^{14}$ cm^{-3} in stoichiometric $CsPbBr_3$ single crystals [23]. We note that at high laser excitation power (≥ 30 mW), $n_x > n_T$ indicating that the carrier recombination is mostly bimolecular in nature and is not limited by traps/defect states. Moreover, the values of n_T in Table 1 do not change significantly for all excitation intensities thereby suggesting that most of the available defect/trap states are completely filled. The origin of the electronic traps in $CsPBr_3$ is tentatively assigned to Br vacancies (V_{Br}), Cs interstitials (Cs_i), and Pb on Cs antisites (Pb_{Cs}) due to our previous DFT calculations as well as calculations in Ref. [11]. These intrinsic native defects introduce transition levels that happen to be located very close to the conduction bandgap edge [11]. These transition levels are usually not carrier trapping centers, making $CsPbBr_3$ a defect tolerant semiconductor [11].

Using the values of b' and τ in Table 1 the bimolecular coefficient for excitons (B/n_T) was calculated to be in the range $3.52 \times 10^{-7} - 5.41 \times 10^{-8}$ cm^3/s for the excitation intensities 10 – 75 mW. For comparison the bimolecular recombination coefficient has been determined for a variety of hybrid metal halide perovskites with values in the range $0.6 \times 10^{-10} - 1.4 \times 10^{-9}$ cm^3 s^{-1} at room temperature [24, 25, 26], which is 1 – 2 orders of magnitudes lower than the values reported here at 15 K. However, the bimolecular recombination constant was reported to increase toward lower temperatures between 3.27×10^{-11} and 1.65×10^{-8} cm^3 s^{-1} for temperatures 310 K to 8 K [26]. The values of τ can also be related to the invariant τ_{ave} from the double exponential fitting in Fig. 2d. From the time derivative of Eq. (7) at $t = 0$, we can write

$$\tau_{ave} = \frac{(1+a)\tau}{(1+b')(1+2a)} \tag{8}$$

Using the values of a and b' from Table 1, it is deduced that $\tau_{ave} \sim \frac{\tau}{10}$, showing that the main contribution for the τ_{ave} is another process with characteristic time much shorter than the

monomolecular decay time . This trend shows that initially, the bimolecular recombination mechanism dominates the TR-PL reduction. At the time scale of , the monomolecular mechanism prevails when the bimolecular term decreases significantly. From Table 1, it can be seen that both parameters and do not change significantly with the intensity of the incident light. Therefore, it is expected that will decrease with the increase of when the power of the incident light increases. This is in agreement with the observed trend, a decrease in lifetime with increasing excitation, shown in Fig. 2d for the double exponential fitting.

It is evident from the results of the fitting that the dominant species for the intensities measured are excitons (with ⩽5% contribution from free photogenerated carriers) as shown in Fig. 4a. Consequently, we focus solely on the exciton dynamics to provide further insight into exciton-exciton interactions and to confirm the findings of our model in eqn. 7. We observe from Fig. 4(b) that the decay time depends strongly on the excitation intensity; a fast decay component becomes prominent with increasing excitation intensity. Such an intensity-dependent decay is not expected from a non-interacting exciton system, thereby indicating strong exciton-exciton interactions that result in their annihilation [27, 28]. Exciton-exciton annihilation has been found to be significant only in the initial times of the decay when the carrier densities are high, while the single-particle process dominates decays at longer time scales with lower densities [21].

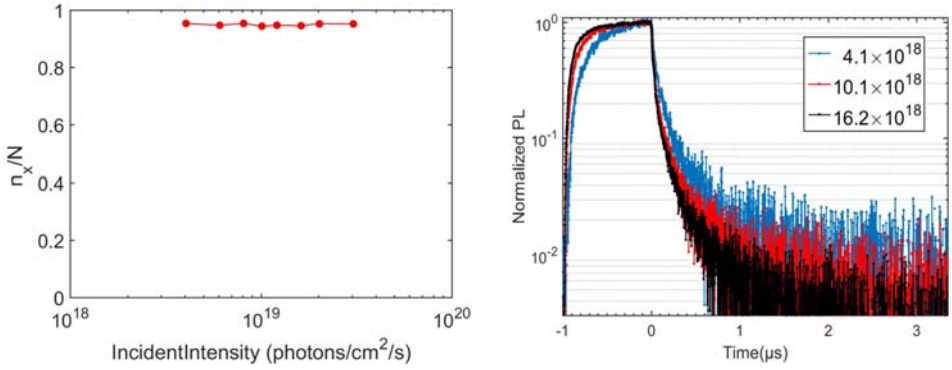

Fig. 4. (a) Ratio of excitons to the number of photogenerated carriers *N*. (b) Exciton decay for increasing excitations (number of photons/cm^2/s).

Based on the fittings results listed in Table 1 and shown in Fig. 4, we postulate exciton-exciton annihilation as a dominant recombination mechanism responsible for the observed nonlinear PL dynamics. Within the framework of exciton interactions, the rate equation for the exciton population n_x can be written as,

$$\frac{dn_x}{dt} = -\frac{n_x}{\tau_x} - \eta n_x^2 \tag{9}$$

where τ_x is the exciton lifetime without annihilation and η is the exciton-exciton annihilation rate constant [24]. We note here that the rate constants η and γ in Eqns. (9) and (1), respectively, are essentially the same. The distinction in nomenclature is to show in a self-consistent way that exciton-exciton interaction dominates the transient PL. η is used when only considering exciton decay while γ is used, however, when considering decay involving both excitons and free carriers. The solution to Eq. (9) is the form

$$n_x(t) = \frac{n_x(0)e^{\left(-\frac{t}{\tau_x}\right)}}{1+\ \eta\tau_x n_x(0)\left[1-e^{\left(-\frac{t}{\tau_x}\right)}\right]}. \tag{10}$$

It can be rewritten as

$$n_x(0)/n_x(t) = [1+\ \eta\tau_x n_x(0)]e^{\left(\frac{t}{\tau_x}\right)} -\ \eta\tau_x n_x(0) \tag{11}$$

with a normalized PL intensity for excitons,

$$\frac{I_{PL}(t)}{I_{PL}(0)} = \frac{e^{\left(-\frac{t}{\tau_x}\right)}}{1+\ \eta\tau_x n_x(0)\left[1-e^{\left(-\frac{t}{\tau_x}\right)}\right]} \tag{12}$$

where I_{PL} (t) denotes the PL intensity and $n_x(0)$ is the initial exciton density.

The normalized PL intensity for different excitations (Fig. 4a) shows that the decay depends strongly on the initially photogenerated density, $n_x(0)$, indicating a strong bimolecular

component. We notice in Fig. 5a that the data before 0.5 µs can be satisfactorily fit with eqn. (12), as indicated by the solid red line. To confirm the dominance of the bimolecular process in this time region a plot of $n_x(0)/n_x(t)$ versus $e^{\left(\frac{t}{\tau_x}\right)}$ and as a function of time is shown in Fig. 5b. In the initial 0.5 µs, the data are consistent with Eq. (11), as indicated by the solid black line. This is an indication that recombination primarily proceeds via a two-body mechanism, namely exciton–exciton annihilation.

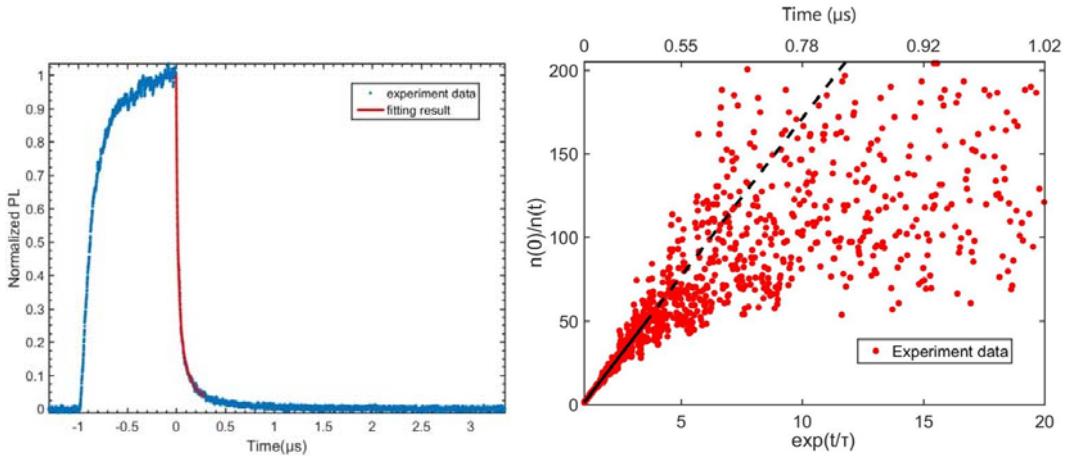

Fig. 5. (a) The decay of PL with time for 40 mW laser excitation. (b) Fit of $n_x(0)/n_x(t)$ versus $e^{\left(\frac{t}{\tau_x}\right)}$ to Eq. (11). The deviation from linearity for $e^{\frac{t}{\tau}} > 4$ may be due to a monomolecular process or to the background noise of the decaying signal.

The deviation from a linear fit (dashed line) after ~0.5 µs may be due to the monomolecular process or to the background noise of the decaying signal. Accordingly, using Eq. (12), we applied a global fit to the whole data set (10 mW – 75 mW) within the time window 0 – 0.5 µs to determine the exciton–exciton annihilation rate η. From the fitting results, the values of annihilation rate constant η range from 3.67×10^{-7} cm^3s^{-1} at 10 mW to an almost constant value of ~2.82×10^{-7} cm^3s^{-1} at and above 30 mW. This value is comparable to a value of 7×10^{-7} cm^3s^{-1} obtained for $CsPbBr_3$ QDs [29]. Moreover, the η values are in agreement with the exciton biomolecular

coefficient obtained using fitting parameters of b' and τ in Table 1. In contrast to the constant lifetime of the single body (monomolecular) process, the pseudo bimolecular lifetime (defined as $\tau_B = [\eta n_x]^{-1}$), is inversely proportional to the excitation intensity. The values of τ_B were calculated to be in the range 56.2 – 22.8 ns from 10 – 75 mW.

Based on the experimental data analyses described above, the decay pathways for $CsPbBr_3$ single crystals involve exciton-exciton recombination and exciton-exciton annihilation. Our model (eqn. 7) predicts that for high photon flux > 10^{18} photons/cm^2/s bimolecular recombination involving excitons is the dominant mechanism for steady state and transient PL. This prediction is supported by the excitonic emission peaks observed in the steady state PL shown in Fig. 2b, as well as those observed in other $CsPbBr_3$ bulk single crystals [16] and $CsPbBr_3$-like quantum dots in CsBr single crystals [17]. Our model also predicts that for increasing photon flux, the exciton-exciton annihilation mechanism becomes prominent leading to a faster characteristic decay time. Finally, with increasing photon flux most of the available defect/trap states become completely filled. Consequently, monomolecular recombination, i.e., recombination via defects/traps does not significantly impact the PL dynamics under high photon flux and the performance potential of the crystal is not affected.

The schematic in Fig. 6 illustrates the described carrier dynamics under photoexcitation in $CsPbBr_3$. Specifically, photoexcitation (1) generates electron-hole pairs, a majority of which form excitons (2a) and electron traps may also be populated (2b). The excitons (2a) can radiatively (3a) and/or non-radiatively recombine or dissociate into free electrons and holes (3b). With increasing intensity, exciton-exciton annihilation occurs. This is a two-exciton interaction process, in which one exciton non-radiatively recombines to the ground state (3c) and the other either

dissociates into free electrons and holes (3b) or is promoted into a higher energy level. The radiative recombination of free electrons and holes (2c) is much weaker than the dominant radiative recombination of excitons (3a). The schematic in Fig. 6 thus provides insight into the nature of the photogenerated carriers at the band-edge of the halide perovskite $CsPbBr_3$.

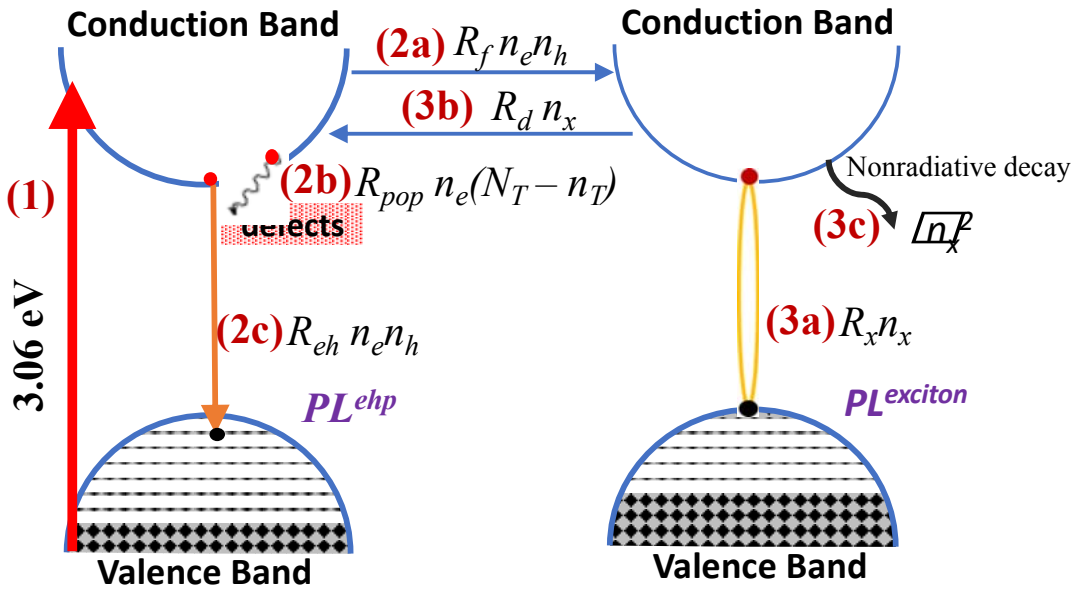

Fig. 6. Schematic of carrier recombination mechanisms in $CsPbBr_3$ single crystals. (1) Photoexcitation; (2a) exciton formation; (2b) trap population; (2c) recombination of free electrons and holes; (3a) exciton recombination; (3b) exciton dissociation; (3c) exciton-exciton annihilation.

IV. CONCLUSION

In summary, the dynamic interactions between free carriers, excitons, and electronic subgap states for stoichiometric $CsPbBr_3$ single crystals have been investigated by means of time-resolved photoluminescence. The concentration of filled traps was calculated, and the origin of the electronic traps in $CsPBr_3$ is tentatively assigned to Br vacancies (V_{Br}), Cs

interstitials (Cs_i), and Pb on Cs antisites (Pb_{Cs}). A recombination model was developed that reproduces the observed PL decay kinetics. At all excitation intensities, recombination of the photogenerated species is dominated by efficient radiative processes involving excitons indicating that the observed steady state PL is a bimolecular process and not strongly influenced by monomolecular recombination (i.e. recombination via defects/traps). A bimolecular recombination coefficient of ~10^{-7} cm^3/s was obtained for a combination of electron-hole pair and exciton recombination. As the concentration of photoexcited charge carriers increases, exciton-exciton annihilation occurs. It is demonstrated that the decreased PL lifetime at high fluence results from exciton–exciton annihilation with annihilation rate of 3.63×10^{-7} cm^3s^{-1} at 10 mW. The observation of an exciton-exciton annihilation process illustrates the strong interaction between excitons in $CsPbBr_3$. Photoluminescence measurements provide fundamental insights into the origin of radiative and nonradiative decay of charge carriers in crystalline $CsPbBr_3$. Having a detailed understanding of free carrier and exciton recombination processes at the band-edge is essential to further our understanding of all-inorganic halide perovskite semiconductors and to reach the ultimate potential of these materials for both radiation detection and optoelectronic applications.

ACKNOWLEDGMENTS

This work was supported by the Department of Homeland Security ARI program with grant no. 2014-DN-077-ARI086-01. This work made use of the Materials Processing and

Microfabrication Facility supported by the MRSEC program of the National Science Foundation (DMR-1720139) at the Materials Research Center of Northwestern University.

* b-wessels@northwestern.edu

References

[1] M. Prokesch, S. A. Soldner, A. G. Sundaram, M. D. Reed, H. Li, J. F. Eger, J. L. Reiber, C. L. Shanor, C. L. Wray, A. J. Emerick, A. F. Peters, IEEE Trans. Nucl. Sci. **63**, 1854 (2016).

[2] C. Szeles, CdZnTe and CdTe Crystals for Medical Applications, in Radiation Detectors for Medical Imaging, Ed. by Iwanczyk JS, CRC Press, 1st edition (2015).

[3] K. Hitomi, T. Onodera, S. Y. Kim, T. Shoji, K. Ishii, Nuclear Instruments and Methods in Physics Research Section A: Accelerators, Spectrometers, Detectors and Associated Equipment **747**, 7 (2014).

[4] S. Yakunin, D. N. Dirin, Y. Shynkarenko, V. Morad, I. Cherniukh, O. Nazarenko, D. Kreil, T. Nauser, M. V. Kovalenko, Nature Photonics **10**, 585 (2016).

[5] Y. He, O. Kontsevoi, C. Stoumpos, G. Trimarchi, S. Islam, Z. Liu, S. Kostina, S. Das, J. Kim, W. Lin, B. Wessels, M. Kanatzidis, J. Am. Chem. Soc. **139**, 7939 (2017).

[6] W. Lin, C. Stoumpos, Z. Liu, S. Das, O. Kontsevoi, Y. He, C. Malliakas, H. Chen, B. Wessels, M. Kanatzidis, ACS Photonics **4**, 1805 (2017).

[7] Y. Xu, X. Fu, H. Zheng, Y. He, W. Lin, K. McCall, Z. Liu, S. Das, B. Wessels, M. Kanatzidis, ACS Photonics **5**, 566 (2017).

[8] Y. He, L. Matei, H. J. Jung, K. M. McCall, M. Chen, C. C. Stoumpos, Z. Liu, J. A. Peters, D. Y. Chung, B. W. Wessels, M. R. Wasielewski, Nature Communications **9**, 1609 (2018).

[9] M. Kulbak, D. Cahen, G. Hodes, The Journal of Physical Chemistry Letters **6**, 2452 (2015).

[10] C. Stoumpos, C. D. Malliakas, J. A. Peters, Z. Liu, M. Sebastian, J. Im, T. C. Chasapis, A. C. Wibowo, D. Y. Chung, A. J. Freeman, B. W. Wessels, M. G. Kanatzidis, Crystal Growth & Design **13**, 2722 (2013).

[11] J. Kang, and L.-W Wang, The Journal of Physical Chemistry Letters **8**, 489 (2017).

[12] O. Brandt, H. Yang, K. H. Ploog, Physical Review B **54**, R5215 (1996).

[13] O. Brandt, J. Ringling, K. H. Ploog, H. J. Wünsche, F. Henneberger, Physical Review B **58**, R15977 (1998).

[14] Pelant I, Valenta J., Luminescence Spectroscopy of Semiconductors. Oxford University Press; 2012.

[15] P. Guo, Y. Xia, J. Gong, C. C. Stoumpos, K. M. McCall, G. C. B. Alexander, Z. Ma, H. Zhou, D. J. Gosztola, J. B. Ketterson, M. G. Kanatzidis, T. Xu, M. K. Y. Chan, R. D. Schaller, ACS Energy Lett. **2**, 2463 (2017).

[16] M. Sebastian, J. A. Peters, C. C. Stoumpos, J. Im, S. S. Kostina, Z. Liu, M. G. Kanatzidis, A. J. Freeman, B. W. Wessels, Physical Review B **92**, 235210 (2015).

[17] M. Nikl, K. Nitsch, E. Mihokova, K. Polak, P. Fabeni, G. P. Pazzi, M. Gurioli, S. Santucci, R. Phani, A. Scacco, F. Somma, Physica E: Low-dimensional Systems and Nanostructures **4**, 323 (1999).

[18] J. H. Cha, J. H. Han, W. Yin, C. Park, Y. Park, T. K. Ahn, J. H. Cho, D. Y. Jung, The Journal of Physical Chemistry Letters **8**, 565 (2017).

[19] S. D. Stranks, V. M. Burlakov, T. Leijtens, J. M. Ball, A. Goriely, H. J. Snaith, Physical Review Applied **2**, 034007 (2014).

[20] J. Szczytko, L. Kappei, J. Berney, F. Morier-Genoud, M. T. Portella-Oberli, and B. Deveaud, Physical Review Letters **93**, 137401 (2004).

[21] N. Kumar, Q. Cui, F. Ceballos, D. He, Y. Wang, H. Zhao, Physical Review B **89**, 125427 (2014).

[22] L. Yuang and L. Huang, Nanoscale **7**, 7402 (2015).

[23] M. Zhang, Z. Zheng, Q. Fu, P. Guo, S. Zhang, C. Chen, H. Chen, M. Wang, W. Luo, Y. Tian, The Journal of Physical Chemistry C **122**, 10309 (2018).

[24] C. Wehrenfennig, G. E. Eperon, M. B. Johnston, H. J. Snaith, L. M. Herz, Advanced Materials **26**, 1584 (2014).

[25] W. Rehman, R. L. Milot, G. E. Eperon, C. Wehrenfennig, J. L. Boland, H. J. Snaith, M. B. Johnston, L. M. Herz, Advanced Materials **27**, 7938 (2015).

[26] R. L. Milot, G. E. Eperon, H. J. Snaith, M. B. Johnston, L. M. Herz, Advanced Functional Materials **25**, 6218 (2015).

[27] L. Huang and T. D. Krauss, Physical Review Letters **96**, 057407 (2006).

[28] H. Htoon, J. A. Hollingsworth, R. Dickerson, V. I. Klimov, Physical Review Letters **91**, 227401 (2003).

[29] K. Wei, X. Zheng, X. Cheng, C. Shen, T. Jiang, Advanced Optical Materials **4**, 1993 (2016).